

Flow physics characterization of microconfined high-pressure transcritical fluids turbulence

By M. Bernades[†], F. Capuano[†], K. Maeda AND L. Jofre[†]

Microfluidics technology has grown rapidly over the past decades due to its high surface-to-volume ratios, flow controllability, and length scales efficiently suited for interacting with microscopic elements. These properties have proven to be well-suited to biology and chemistry, in which localized precision is usually an advantage. However, as a consequence of the small rates of mixing and transfer they achieve due to operating under laminar (smooth) flow regimes, the utilization of microfluidics for energy applications has long been a key challenge. In this regard, as a result of the thermophysical properties they exhibit in the vicinity of the pseudo-boiling region, it has been recently proposed that microconfined turbulence could be achieved by operating at high-pressure transcritical fluid conditions. However, the underlying flow mechanisms of such systems are still not well characterized and thus need to be carefully investigated. Consequently, this work analyzes supercritical microconfined turbulence by computing direct numerical simulations of high-pressure ($P/P_c = 2$) N_2 at transcritical temperature conditions imposed by a temperature difference between the bottom ($T/T_c = 0.75$) and top ($T/T_c = 1.5$) walls for a friction Reynolds number of $Re_\tau = 100$ (bottom wall). The results obtained indicate that microconfined turbulence can be achieved under such conditions, leading to transfer increments up to $20\times$ those that occur in equivalent low-pressure configurations.

1. Introduction

Enhancing mixing and transfer rates in microfluidic devices has been a notable challenge over the past decades. In general, microfluidic systems are characterized by hydraulic diameters in the range $D_h \sim 1 - 1000 \mu\text{m}$ and operate at average velocities of $u_b \sim \mathcal{O}(1)$ m/s and smaller. As a result, the Reynolds numbers achieved in most standard microfluidic systems are on the order of $Re = uL/\nu \sim 0.1 - 100$, with u and L the characteristic velocity and length scales, respectively, and ν the kinematic viscosity of the fluid. Consequently, standard fluids at atmospheric conditions are not able to reach turbulent regimes in microfluidic systems as their kinematic viscosities are typically in the range $\nu \sim 10^{-6} - 10^{-4} \text{ m}^2/\text{s}$ and thus viscous forces dominate over inertial effects. The smooth nature of this flow regime does not provide good mixing and transfer efficiencies in comparison to the performances obtained if turbulence, which is characterized by rapid fluctuations of flow variables in time and space, is present. Instead, in most macroscale energy applications, for example related to power and heat transfer, turbulence is a key mechanism for achieving high levels of performance and efficiency due to the notable increase in mixing and transfer rates that it provides (Sreenivasan 2019). While there is no general theorem relating Re to a laminar/turbulent flow regime, flows at Re larger than 4000–5000 are typically (but not necessarily) turbulent, while those at low Re usually remain laminar. In internal flows, for example, turbulence can be sustained if Re is larger than a critical value of approximately 2300 (Pope 2000).

[†] Universitat Politècnica de Catalunya, BarcelonaTech (UPC), Spain

Although several research groups have attempted to overcome this frontier by employing different techniques such as electrokinetic forcing (Wang *et al.* 2016; Nan *et al.* 2020) or increasing the volumetric flow rate (large sizes/velocities) in microdevices to reach incipient turbulent flow conditions (Sharp & Adrian 2004; Wibel & Ehrhard 2009; You *et al.* 2015), turbulent states in microconfined devices have not yet been achieved. To this extent, a drastically different approach is based on directly developing turbulent flow in microfluidic systems by means of leveraging the properties of supercritical fluids at transcritical conditions (Jofre & Urzay 2020, 2021). In particular, the strategy proposed in this work makes use of the rapid smooth transition when crossing the pseudo-boiling line to tune supercritical fluids to present liquid-like densities ($\rho \sim 10^3 \text{ kg/m}^3$) and gas-like viscosities ($\mu \sim 10^{-5} \text{ Pa}\cdot\text{s}$), and therefore achieve $Re \sim 10^3\text{--}10^4$ for typical microfluidic velocities and channel sizes, therefore favoring inertial over viscous forces and resulting in turbulent flow (Bernades & Jofre 2022).

The flow physics complexity of supercritical fluids across the pseudo-boiling region typically leads to poor prediction capabilities of Reynolds-averaged Navier-Stokes (RANS) simulation approaches (Yoo 2013). Consequently, the coupled hydrodynamic and thermal behavior of high-pressure transcritical turbulence, for example in terms of the enhancement and deterioration of heat transfer, cannot be captured correctly. In this regard, scale-resolving methodologies based on direct numerical simulation (DNS) and large eddy simulation (LES) are typically required to properly characterize and/or predict high-pressure transcritical turbulent flows. Selected examples of scale-resolving studies include (i) DNS of supercritical heat transfer in pipe flows by Bae *et al.* (2005, 2008); (ii) DNS of transcritical flows close to the critical point by Sengupta *et al.* (2017); (iii) LES and DNS of transcritical channel flows by Doehring *et al.* (2021) and Ma *et al.* (2018), respectively; and (iv) DNS of transcritical turbulent boundary layers by Kawai (2019).

Therefore, the objectives of this study are (i) to explore the capability of supercritical fluids to achieve microconfined turbulence, and (ii) to characterize the corresponding flow physics. In this regard, the work is organized as follows. First, in Section 2, the flow physics modeling of supercritical fluids is described together with the novel numerical scheme utilized. Next, the computational results are presented and analyzed in Section 3. Finally, the work is concluded and future directions are proposed in Section 4.

2. Flow physics and numerical modeling

The framework utilized for studying microconfined high-pressure transcritical turbulence in terms of (i) equations of fluid motion, (ii) real-gas thermodynamics, (iii) high-pressure transport coefficients, and (iv) numerical scheme is described below.

2.1. Equations of fluid motion

The turbulent flow motion of supercritical fluids is described by the following set of conservation equations of mass, momentum, and pressure

$$\frac{\partial \rho}{\partial t} + \nabla \cdot (\rho \mathbf{v}) = 0, \quad (2.1)$$

$$\frac{\partial (\rho \mathbf{v})}{\partial t} + \nabla \cdot (\rho \mathbf{v} \mathbf{v}) = -\nabla P + \nabla \cdot \boldsymbol{\tau}, \quad (2.2)$$

$$\frac{\partial P}{\partial t} + \mathbf{v} \cdot \nabla P + \rho c^2 \nabla \cdot \mathbf{v} = \frac{1}{\rho} \frac{\beta_v}{c_v \beta_T} (\boldsymbol{\tau} : \nabla \otimes \mathbf{v} - \nabla \cdot \mathbf{q}), \quad (2.3)$$

where ρ is the density, \mathbf{v} is the velocity vector, P is the pressure, $\boldsymbol{\tau}$ is the viscous stress tensor, c is the speed of sound, β_v is the volume expansivity, c_v is the isochoric specific heat, β_T is the isothermal compressibility, and \mathbf{q} is the Fourier heat conduction.

2.2. Real-gas thermodynamics

The thermodynamic space of solutions for the state variables pressure P , temperature T , and density ρ of a single substance is described by an equation of state. One popular choice for systems at high pressures, which is used in this study, is the Peng & Robinson (1976) equation of state written as

$$P = \frac{R_u T}{\bar{v} - b} - \frac{a}{\bar{v}^2 + 2b\bar{v} - b^2}, \quad (2.4)$$

with R_u the universal gas constant, $\bar{v} = W/\rho$ the molar volume, and W the molecular weight. The coefficients a and b take into account real-gas effects related to attractive forces and finite packing volume, respectively, and depend on the critical temperatures T_c , critical pressures P_c , and acentric factors ω . They are defined as

$$a = 0.457 \frac{(R_u T_c)^2}{P_c} \left[1 + c \left(1 - \sqrt{T/T_c} \right) \right]^2 \quad \text{and} \quad b = 0.078 \frac{R_u T_c}{P_c}, \quad (2.5)$$

where coefficient c is provided by

$$c = \begin{cases} 0.380 + 1.485\omega - 0.164\omega^2 + 0.017\omega^3 & \text{if } \omega > 0.49, \\ 0.375 + 1.542\omega - 0.270\omega^2 & \text{otherwise.} \end{cases} \quad (2.6)$$

The Peng-Robinson real-gas equation of state needs to be supplemented with the corresponding high-pressure thermodynamic variables based on departure functions (Reynolds & Colonna 2019) calculated as a difference between two states. In particular, their usefulness is to transform thermodynamic variables from ideal-gas conditions (low pressure: only temperature dependant) to supercritical conditions (high pressure). The ideal-gas parts are calculated by means of the NASA 7-coefficient polynomial (Burcat & Ruscic 2005), while the analytical departure expressions to high pressures are derived from the Peng-Robinson equation of state as detailed in Jofre & Urzay (2021).

2.3. High-pressure transport coefficients

The high pressures involved in the analyses conducted in this work prevent the use of simple relations for the calculation of the dynamic viscosity μ and thermal conductivity κ . In this regard, standard methods for computing these coefficients for Newtonian fluids are based on the correlation expressions proposed by Chung *et al.* (1984, 1988). These correlation expressions are mainly functions of critical temperature T_c and density ρ_c , molecular weight W , acentric factor ω , association factor κ_a and dipole moment \mathcal{M} , and the NASA 7-coefficient polynomial (Burcat & Ruscic 2005); further details can be found in dedicated works such as those of Poling *et al.* (2001) and Jofre & Urzay (2021).

2.4. Numerical scheme

The equations of fluid motion introduced in Section 2.1 are numerically solved by adopting a standard semi-discretization procedure, i.e., they are firstly discretized in space and then integrated in time. In particular, spatial operators are treated using second-order differentiation, and time-integration is performed by means of a third-order strong stability-preserving (SSP) Runge-Kutta explicit scheme (Gottlieb *et al.* 2001). The discretization of the convection terms is based on a stable kinetic energy-preserving scheme,

initially assessed in a previous work (Bernades *et al.* 2022), such that kinetic energy is globally preserved by convection (Coppola *et al.* 2019). In addition, pressure is transported instead of energy to remove spurious oscillations from the numerical solution.

3. Computational results

Microconfined high-pressure transcritical turbulence is studied by means of DNS strategies based on the flow physics framework described in Section 2. Results are obtained utilizing the in-house MPI+OpenACC compressible flow solver RHEA (Jofre & Oyarzún 2020). The problem setup and discussion of flow physics are discussed below.

3.1. Problem setup

The fluid selected to study and characterize high-pressure transcritical fluid turbulence is N_2 , whose critical pressure and temperature are $P_c = 3.4$ MPa and $T_c = 126.2$ K, respectively. The fluid system is at a supercritical bulk pressure of $P_b/P_c = 2$ and is confined between bottom (bw) and top (tw) isothermal walls, separated at a distance $H = 2\delta$ with $\delta = 100$ μm the channel half-height, at $T_{bw}/T_c = 0.75$ and $T_{tw}/T_c = 1.5$, respectively. This problem setup makes the fluid undergo a transcritical trajectory by operating within a thermodynamic region across the pseudo-boiling line. The friction Reynolds number selected at the bottom wall is $Re_{\tau,bw} = \rho_{bw}u_{\tau,bw}\delta/\mu_{bw} = 100$ to ensure fully turbulent flow conditions; the values of ρ_{bw} and μ_{bw} are obtained from the thermophysical model described in Section 2. The mass flow rate in the streamwise direction is imposed through a body force controlled by a feedback loop coupled to a proportional controller (gain $k_p = 0.1$) aimed at reducing the difference between the desired ($Re_{\tau,bw} = 100$) and measured (numerical) $Re_{\tau,bw}$ values.

The computational domain is $4\pi\delta \times 2\delta \times 4/3\pi\delta$ in the streamwise (x), wall-normal (y), and spanwise (z) directions, respectively. The streamwise and spanwise boundaries are set periodic, and no-slip conditions are imposed on the horizontal boundaries (x - z planes). The grid is uniform in the streamwise and spanwise directions, with resolutions in wall units (based on bw values) equal to $\Delta x^+ \approx 9.8$ and $\Delta z^+ \approx 3.3$ and stretched toward the walls in the vertical direction with the first grid point at $y^+ = yu_{\tau,bw}/\nu_{bw} \approx 0.1$ and with sizes in the range $0.2 < \sim \Delta y^+ < \sim 2.3$. Thus, this grid arrangement corresponds to a DNS of size $128 \times 128 \times 128$ grid points. The simulation strategy starts from a linear velocity profile with random fluctuations (Nelson & Fringer 2017), which is advanced in time to reach turbulent steady-state conditions after approximately 5 flow-through-time (FTT) units; based on the bulk velocity u_b and the length of the channel $L_x = 4\pi\delta$, a FTT is defined as $t_b = L_x/u_b \sim \delta/u_{\tau}$. In this regard, flow statistics are collected for roughly 10 FTTs once steady-state conditions are achieved.

3.2. Turbulent flow statistics

The time-averaged streamwise velocity u^+ and Favre-averaged root-mean-squared (rms) velocity fluctuations u_{rms}^+ , v_{rms}^+ and w_{rms}^+ along the wall-normal direction y^+ in viscous units for the bottom and top walls are depicted in Figure 1 up to y^+ , where the maximum streamwise velocity is located ($y/\delta = 1.03$ from the bottom wall). Two main results can be inferred from these plots. First, as shown in Figure 1(a), the shape of the time-averaged u^+ profiles tends to follow the topology of turbulent boundary layers for the bottom and top walls. However, the profiles do not exactly collapse to the curves (black lines) corresponding to the law of the wall (LoW) for an incompressible flat plate. An interesting observation is that neither do the profiles collapse to the standard law when

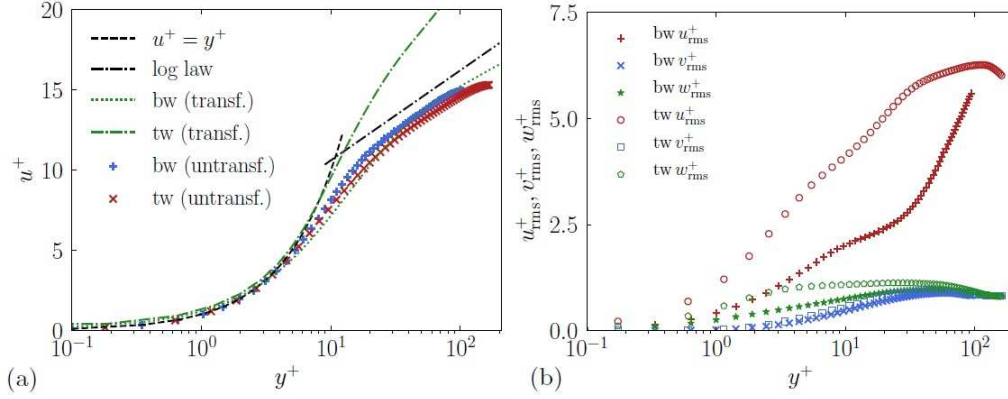


FIGURE 1. (a) Time-averaged streamwise velocity u^+ and (b) Favre-averaged rms velocity fluctuations u_{rms}^+ , v_{rms}^+ and w_{rms}^+ along the y^+ direction for bottom (bw) and top walls (tw).

utilizing the state-of-the-art transformation proposed by Trettel & Larsson (2016), which was developed for non-isothermal compressible boundary layers. Although this transformation results in accurate agreement for other high-pressure transcritical flows, such as the study performed by Toki & Teramoto (2020), the relatively low Reynolds numbers of the case studied in this work, in combination with a sustained baroclinic instability that appears close to the top wall, forces the turbulent flow to significantly deviate from traditional wall-turbulence behavior. To this extent, Section 3.4 explores the sources for this observed flow physics behaviour. Second, focusing on the Favre-averaged rms velocity fluctuations shown in Figure 1(b), turbulence intensity is significantly different between the top (gas-like) and bottom (liquid-like) walls. In particular, the top wall presents larger fluctuations in the viscous sublayer and buffer region, while turbulence intensity grows following a concave parabola from the bottom wall to the center of the channel. An equivalent, although significantly less pronounced, behavior is observed for the fluctuations in the wall-normal velocity, whereas they virtually collapse to the same curve for the spanwise direction.

3.3. Comparison against atmospheric pressure conditions

A low-pressure channel flow case equivalent to the high-pressure system is computed to compare the mixing and heat transfer rate when operating at transcritical regimes with respect to atmospheric (low-pressure) conditions. This low-pressure setup is defined by providing the same volumetric power input [i.e., $u_b(-dP/dx) = u_b(\tau_{w,b} + \tau_{w,t})/2\delta$] to the fluid as in the transcritical case to compare equivalent energized flows. In this regard, the mass flow rate in the streamwise direction is imposed through a body force controlled by a feedback loop, which in this case aims to reduce the difference between the desired and measured volumetric power input. However, the main difference is introduced by reducing the operating bulk pressure to $P_b/P_c = 0.03$. To this extent, a low-pressure framework is utilized based on the ideal-gas equation of state and the Sutherland (1983) law for the transport coefficients, viz. dynamic viscosity and thermal conductivity. A snapshot of the instantaneous streamwise velocity in wall units u^+ on a y - z slice is displayed in Figure 2. The figure provides qualitative information of the wall-bounded turbulence and highlights the strong turbulence intensity of the transcritical case in comparison to the laminarized low-pressure setup.

Table 1 quantifies the difference in dimensionless numbers for both setups at each

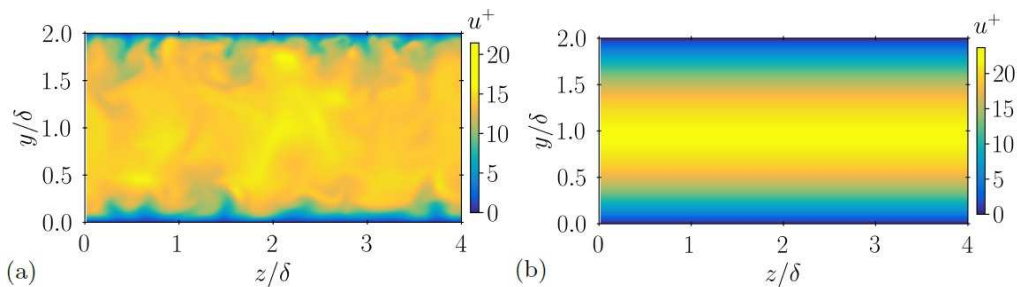


FIGURE 2. Snapshot of instantaneous streamwise velocity in wall units u^+ on a y - z slice for (a) transcritical and (b) low pressure conditions at same volumetric power input.

		Re_τ	C_f	Pr	Nu	St
Transcritical	Top	179.9	0.003	0.97	22.0	0.13
	Bottom	100.0	0.020	2.14	5.61	0.03
Low pressure	Top	22.60	0.022	0.73	0.85	0.051
	Bottom	49.17	0.014	0.78	1.37	0.036

TABLE 1. Dimensionless numbers for (i) transcritical and (ii) low-pressure conditions.

wall. From this information, the five following observations can be noted. First, as characterized by the friction Reynolds number Re_τ , the transcritical channel flow presents larger turbulent fluctuations at the top wall in comparison to the bottom wall. Instead, at low-pressure conditions, the flow becomes laminar, as summarized by Bernades & Jofre (2022). Second, the skin-friction coefficient C_f is an order of magnitude smaller at the top wall with respect to the bottom wall for the transcritical case while it is of the same order for the low-pressure system. Third, the Prandtl number Pr is approximately $2\times$ larger at the bottom wall for the high-pressure case, and presents virtually no difference between walls at low-pressure conditions. Fourth, the Nusselt number Nu , which quantifies the heat transfer enhancement by convection with respect to conduction, presents an increase of roughly $20\times$ for the transcritical system with respect to the low pressure case. Finally, for the transcritical setup, the Stanton number St , which measures the ratio of heat transferred into a fluid to the thermal capacity of the fluid, is an order of magnitude larger at the top than at the bottom wall. Importantly, these results computationally corroborate the hypothesis that microconfined turbulent flow can be achieved when operating at high-pressure transcritical regimes, and consequently significantly larger values of flow mixing and heat transfer rates with respect to similar microchannels at atmospheric pressure conditions can be potentially obtained.

3.4. Turbulence sources and topology

As previously introduced in Section 3.2, turbulent flow statistics differ substantially from the standard incompressible turbulent channel flow case. One of the underlying physical mechanisms responsible for such differences is the presence of a significantly localized baroclinic instability close to the top wall. In particular, the instability, which is generated by the combination of (i) the external force driving the flow in the streamwise direction

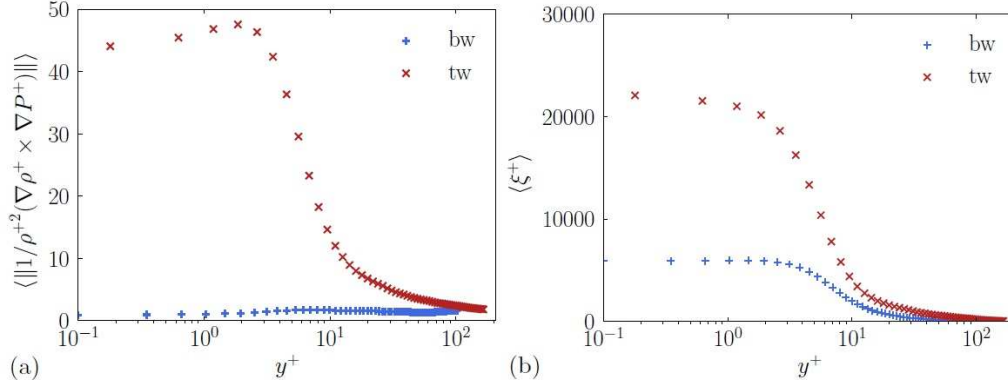


FIGURE 3. Ensemble-averaged values of (a) baroclinic torque and (b) enstrophy in wall units along the wall-normal direction for bottom (bw) and top walls (tw).

and (ii) the density gradient across the pseudo-boiling region in the wall-normal direction, is responsible for injecting vorticity with a peak value located in the vicinity of the top wall at $y^+ \approx 5$, as depicted in Figure 3(a). As a result, notably higher levels of enstrophy are observed near the top wall (values approximately $10\times$ larger) in comparison to the bottom wall, as quantified in Figure 3(b). Enstrophy is also produced by the friction of the fluid with the walls due to shear stresses. However, the presence of this baroclinic torque induces larger enstrophy values close to the top wall, which result in higher levels of flow fluctuations in the top region of the channel.

The Q -criterion (Dubief & Delcayre 2000) is utilized to further characterize the small scales of the flow. In this regard, the second invariant Q_A of the velocity-gradient tensor $A_{ij} = \partial u_i / \partial x_j$, which can be decomposed into symmetric S_{ij} (rate-of-strain) and skew-symmetric Ω_{ij} (rate-of-rotation) parts, is calculated as

$$Q_A = \frac{1}{2} [\text{tr}(A_{ij})^2 - \text{tr}(A_{ij}^2)] = \frac{1}{2} (P_A^2 - S_{ij}S_{ji} - \Omega_{ij}\Omega_{ji}), \quad (3.1)$$

where $P_A = -\text{tr}(A_{ij}) = -S_{ii}$ is the first invariant. This quantity is a measure of the relative importance of the straining and rotational parts of the velocity-gradient tensor. Hence, in regions in which Q_A is large and positive, vorticity is high and dominates strain rate, while if it is large and negative, vorticity is no longer dominant (Dodd & Jofre 2019). The ensemble-averaged, i.e., spatially averaged utilizing 10 samples, values of normalized $Q_A^+ = Q_A(H/u_b)^2$ along the wall-normal direction are shown in Figure 4(a). As can be observed, vorticity is dominant for most of the wall-normal direction, as Q_A presents positive values with a peak at $y/\delta \approx 1.88$. However, Q_A shows a rapid variation to negative large values with a minimum at $y/\delta = 1.98$, indicating that strain rate prevails in the vicinity of the top wall. This location corresponds to the wall-normal position where there is a peak in density gradient due to crossing the pseudo-boiling region.

Finally, the barycentric map (Banerjee *et al.* 2007), as depicted in Figure 4(b), qualitatively characterizes the anisotropy of the turbulent flow. The barycentric map enables the visual representation of the three limiting states of turbulence, corresponding to turbulent fluctuations dominant in (i) one (rod-like, x_{1c}), (ii) two (disk-like, x_{2c}), and (iii) three (spherical, x_{3c}) directions. As shown by the map, the flow fluctuates mainly in two directions at the bottom and top walls (two-component limit); viz. the fluid is bounded in y but allowed to fluctuate in x and z . However, the turbulent stresses follow a concave

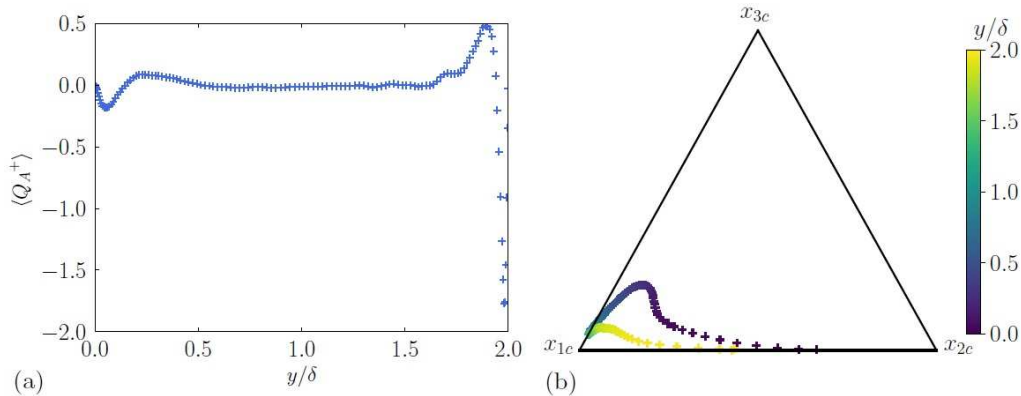


FIGURE 4. Evolution of (a) ensemble-averaged Q_A^+ and (b) Favre-averaged flow stresses on the barycentric map (b) along the wall-normal direction.

trajectory toward the one-component state in the vicinity of the axisymmetric expansion region when approaching the center of the channel. In particular, in that region, the flow tends to fluctuate mostly in the streamwise direction, as shown in Figure 1(b).

4. Conclusions

The DNS results obtained in this work demonstrate the feasibility of achieving microconfined turbulence by leveraging the thermophysical properties of supercritical fluids. To that end, the results are compared to an equivalent low-pressure (atmospheric conditions) setup to (i) characterize the differences in flow statistics and (ii) quantify the mixing and heat transfer enhancement with respect to standard microfluidic laminar flow regimes. In particular, even though the first-order flow statistics follow the topology of turbulent boundary layers, (i) they do not collapse exactly to the standard LoW, and (ii) the streamwise velocity fluctuations differ significantly between the bottom and top walls. These differences are mainly driven by a baroclinic instability introducing vorticity in the vicinity of the top wall, which is generated from the interaction of the external force driving the flow in the streamwise direction and the density gradient across the pseudo-boiling region in the wall-normal direction.

In this regard, the interesting and rich flow phenomena observed in the initial set of results presented in this work motivate the authors to continue studying the complex flow physics of microconfined turbulence at high-pressure transcritical conditions. In particular, focus in the mid-term will be placed on (i) analyzing the near-wall flow behavior, (ii) characterizing the baroclinic instability, and (iii) investigating the flow structures.

Acknowledgements

The authors acknowledge use of computational resources from the Yellowstone cluster awarded by the National Science Foundation to CTR.

REFERENCES

- BAE, J. H., YOO, J. Y. & CHOI, H. 2005 Direct numerical simulation of turbulent supercritical flows with heat transfer. *Phys. Fluids* **17**, 105104.
- BAE, J. H., YOO, J. Y. & MCELIGOT, D. M. 2008 Direct numerical simulation of

- heated CO_2 flows at supercritical pressure in a vertical annulus at $Re = 8900$. *Phys. Fluids* **20**, 055108.
- BANERJEE, S., KRAHL, R., DURST, F. & ZENGER, C. 2007 Presentation of anisotropy properties of turbulence, invariants versus eigenvalue approaches. *J. Turbul.* **8**, N32.
- BERNADES, M., CAPUANO, F., TRIAS, F. X. & JOFRE, L. 2022 Energy-preserving stable computations of high-pressure supercritical fluids turbulence. In *9th European Congress on Computational Methods in Applied Sciences and Engineering (ECCOMAS)*, pp. 1–12.
- BERNADES, M. & JOFRE, L. 2022 Thermophysical analysis of microconfined turbulent flow regimes at supercritical fluid conditions in heat transfer applications. *J. Heat Transf.* **144**, 082501.
- BURCAT, A. & RUSCIC, B. 2005 Third millennium ideal gas and condensed phase thermochemical database for combustion with updates from active thermochemical tables. *Tech. Rep.*, Argonne National Laboratory.
- CHUNG, T. H., AJLAN, M., LEE, L. L. & STARLING, K. E. 1988 Generalized multi-parameter correlation for nonpolar and polar fluid transport properties. *Ind. Eng. Chem. Res.* **27**, 671–679.
- CHUNG, T. H., LEE, L. L. & STARLING, K. E. 1984 Applications of kinetic gas theories and multiparameter correlation for prediction of dilute gas viscosity and thermal conductivity. *Ind. Eng. Chem. Res.* **23**, 8–13.
- COPPOLA, G., CAPUANO, F., PIROZZOLI, S. & DE LUCA, L. 2019 Numerically stable formulations of convective terms for turbulent compressible flows. *J. Comput. Phys.* **382**, 86–104.
- DODD, M. & JOFRE, L. 2019 Small-scale flow topologies in decaying isotropic turbulence laden with finite-size droplets. *Phys. Rev. Fluids* **4**, 064303.
- DOEHRING, A., KALLER, T., SCHMIDT, S. J. & ADAMS, N. A. 2021 Large-eddy simulation of turbulent channel flow at transcritical states. *Int. J. Heat Fluid Flow* **89**, 108781.
- DUBIEF, Y. & DELCAYRE, F. 2000 On coherent-vortex identification in turbulence. *J. Turbul.* **1**, N11.
- GOTTLIEB, S., SHU, C.-W. & TADMOR, E. 2001 Strong stability-preserving high-order time discretization methods. *SIAM Review* **43**, 89–112.
- JOFRE, L. & OYARZÚN, G. 2020 RHEA - an open-source Reproducible and Hybrid-architecture flow solver Engineered for Academia. <https://gitlab.com/ProjectRHEA/flowsolverrhea>
- JOFRE, L. & URZAY, J. 2020 A characteristic length scale for density gradients in supercritical monocomponent flows near pseudoboiling. *Annual Research Briefs*, Center for Turbulence Research, Stanford University, pp. 277–282.
- JOFRE, L. & URZAY, J. 2021 Transcritical diffuse-interface hydrodynamics of propellants in high-pressure combustors of chemical propulsion systems. *Prog. Energy Combust. Sci.* **82**, 100877.
- KAWAI, S. 2019 Heated transcritical and unheated non-transcritical turbulent boundary layers at supercritical pressures. *J. Fluid Mech.* **865**, 563–601.
- MA, P. C., YANG, X. I. A. & IHME, M. 2018 Structure of wall-bounded flows at transcritical conditions. *Phys. Rev. Fluids* **3**, 034609.
- NAN, K., HU, Z., ZHAO, W., WANG, K., BAI, J. & WANG, G. 2020 Large-scale flow in micro electrokinetic turbulent mixer. *Micromachines* **11**, 813.

- NELSON, K. S. & FRINGER, O. B. 2017 Reducing spin-up time for simulations of turbulent channel flow. *Phys. Fluids* **29**, 105101.
- PENG, D. Y. & ROBINSON, D. B. 1976 A new two-constant equation of state. *Ind. Eng. Chem. Fundam.* **15**, 59–64.
- POLING, B. E., PRAUSNITZ, J. M. & O'CONNELL, J. P. 2001 *Properties of Gases and Liquids*, 5th ed. McGraw Hill, New York.
- POPE, S. B. 2000 *Turbulent Flows*. Cambridge University Press, Cambridge (UK).
- REYNOLDS, W. C. & COLONNA, P. 2019 *Thermodynamics: Fundamentals and Engineering Applications*, 1st ed. Cambridge University Press, Cambridge (UK).
- SENGUPTA, U., NEMATI, H., BOERSMA, B. J. & PECNIK, R. 2017 Fully compressible low-Mach number simulations of carbon-dioxide at supercritical pressures and trans-critical temperatures. *Flow Turbul. Combust.* **99**, 909–931.
- SHARP, K. V. & ADRIAN, R. J. 2004 Transition from laminar to turbulent flow in liquid filled microtubes. *Exp. Fluids* **36**, 741–747.
- SREENIVASAN, K. R. 2019 Turbulent mixing: a perspective. *PNAS* **116**, 18175–18183.
- SUTHERLAND, W. 1983 LII. the viscosity of gases and molecular force. *Lond. Edinb. Dublin Philos. Mag. J. Sci.* **36**, 507–531.
- TOKI, T. & TERAMOTO, S. 2020 Velocity and temperature profiles in turbulent channel flow at supercritical pressure. *J. Propuls. Power* **36**, 3–13.
- TRETTEL, A. & LARSSON, J. 2016 Mean velocity scaling for compressible wall turbulence with heat transfer. *Phys. Fluids* **28**, 026102.
- WANG, G. R., YANG, F. & ZHAO, W. 2016 Microelectrokinetic turbulence in microfluidics at low Reynolds number. *Phys. Rev. E* **93**, 013106.
- WIBEL, W. & EHRHARD, P. 2009 Experiments on the laminar/turbulent transition of liquid flows in rectangular microchannels. *Heat Transf. Eng.* **30**, 70–77.
- YOO, J. Y. 2013 The turbulent flows of supercritical fluids with heat transfer. *Annu. Rev. Fluid Mech.* **45**, 495–525.
- YOU, J. B., KANG, K., TRAN, T. T., PARK, H., HWANG, W. R., KIM, J. M. & IM, S. G. 2015 PDMS-based turbulent microfluidic mixer. *Lab Chip* **15**, 1727.